

## Surface chiral Berry plasmons on disordered permalloys

Zhen Liang<sup>1</sup> and Tianyu Liu<sup>1,2,\*</sup>

<sup>1</sup>Department of Physics and Center for Joint Quantum Studies, School of Science, Tianjin University, Tianjin 300350, China

<sup>2</sup>Tianjin Key Laboratory of Low Dimensional Materials Physics and Preparing Technology, Tianjin 300350, China



(Received 8 February 2023; revised 30 May 2023; accepted 13 June 2023; published 26 June 2023)

We investigate the surface plasmons propagating on disordered bulk permalloys (Pys), whose magnetization breaks the time reversal symmetry, causing the surface plasmons to possess chirality in the absence of magnetic fields under the interplay of the anomalous Hall conductivity (AHC) and the boundary conditions at the surface. Based on the collisionless hydrodynamic model, we incorporate the effect of interband transitions into the dispersion of surface plasmons. As we show, the AHC will split the forward and backward propagating surface plasmons into two modes, while the  $p$ - $d$  transitions in bulk Py will work against the AHC, yielding slower propagation surface chiral Berry plasmons (CBPs), and even ceasing the presence of surface modes. The resulting surface CBP has a broad bandwidth ranging from visible light to infrared frequency. The free-field chirality may provide a new knob to control the chiral transport of light, as well as a new probe for detecting the intrinsic AHC in ferromagnetic metals.

DOI: [10.1103/PhysRevB.107.224426](https://doi.org/10.1103/PhysRevB.107.224426)

### I. INTRODUCTION

The renewed interest in surface plasmons (SPs) stems primarily from their ability to concentrate light within sub-wavelength structures, accomplished through the formation of surface-plasmon polaritons (SPPs). These SPPs have found widespread applications in the field of plasmonics [1,2]. Recent research in this area encompasses various intriguing aspects, including the excitations of SPs through electric currents [3,4] and stimulated emission of radiation (spasers) [5,6], the development of nanometer-scale photonic circuits [7,8], the generation and manipulation of electromagnetic radiation spanning microwave to optical frequencies [9–12], and the fabrication of subwavelength structure on surfaces using SP-based nanolithography [13]. Additionally, the easy interaction of SPs with light opens up avenues for optically probing the electronic band structures of novel topologically nontrivial two-dimensional materials, such as graphene moiré superlattices [14,15] and  $\alpha$ - $T_3$  lattices [16–18].

Furthermore, recent developments propose the chiral transport of light in Dirac fermion systems through the formation of topologically protected edge SPPs. Combining the feature of Dirac fermions and superlattices, two groups, Pan *et al.* [19] and Jin *et al.* [20], independently proposed to realize topological optical states in graphene superlattice structure via Dirac plasmons that exhibit substantial nonreciprocal behavior, without seeking sophisticated bulky structural designs such as reciprocal metamaterials and photonic crystals. In the presence of periodic structure (i.e., superlattice) the plasmon dispersion exhibits band structure with Dirac points due to the symmetry of the superlattice. As in electron band structure, an applied magnetic field can therefore open a gap at the Dirac

points and lead to topological protected edge plasmon modes. They expect this structured graphene sensible in the infrared regime, in contrast to the bulky structures that often work in microwave regime and have limited feasibility in nanoscale optical integration.

The key ingredient to produce chirality is to have broken time-reversal (TR) symmetry, either by external magnetic fields or by magnetization of the systems. So far, we have discussed the chiral plasmon modes induced by external magnetic fields. The presence of magnetization can also induce chiral plasmon.

Song and Rudner [21] (SR) name a new class of plasmons in 2D metallic system including gapped Dirac materials as chiral Berry plasmons (CBPs). The chirality manifest itself as splitting the oppositely propagating plasmons into two modes, even in the absence of topological edge states. As long as the Bloch bands possess Berry curvature, there is no need for external magnetic fields, which is of particular interest for “on-chip” applications that requires nonreciprocity, such as optical isolators [22,23] and chiral spintronics [24]. Therefore a wide range of metals exhibiting anomalous and quantum anomalous Hall effects can be good platforms for exploring CBPs. Permalloy is among such metals.

FeNi alloys belong to the most important soft magnetic alloy systems. Ni-rich FeNi alloys are called permalloys (Pys) [25]. Most of the studies on Py are dedicated to the effects of spin-orbit torque [26], exchange coupling [27], spin pumping [28] and spin to charge conversion [29] in layered heterostructures. With the arise of topological insulators, the nontrivial topology become a new field in the study of Pys. The studies fall into two categories, the formation of textured magnetization such as vortex or antivortex in Py heterostructures [30], or the magnetotransport properties of Py in different nanopatterns tailored by lithographic printing [31–34], but all of these nontrivial topologies are in real space.

\*tianyu\_liu@tju.edu.cn

In this paper, we study the effect of anomalous Hall conductivity (AHC) caused by the Berry curvature of band structure on the surface plasmons propagating on a disordered bulk Py. In a pioneered paper by Zhang and Vignale [35], the surface CBP on a ferromagnetic conductor has been studied. They used the collisionless hydrodynamic equations together with the Poisson equation to solve the dispersion of the surface plasmons. However, the conduction electrons were treated as nearly free of lattice potential, so that the induced density can only undergo intraband transitions in response to the electric field. In the long wavelength limit, such a treatment converges to the Drude model, leading to the intraband dielectric function. In this work, we apply the  $s$ - $d$  polarization model to study the effect of interband transition, which is indispensable for the disordered Pys, whose  $d$  bands are partially occupied, resulting in an onset frequency of interband transition slightly below the long wavelength surface plasmon frequency.  $d$  electrons behave obviously differently from those in the Drude model, such that they are particularly strongly polarized in the surface region where the surface plasmon's electric field varies rapidly along the surface normal. We simplified the models by treating the  $d$  electrons as a polarizable medium characterized by the local dielectric function  $\epsilon_d(\omega)$ , which reflects the interband transitions in the bulk, as has been applied in the study of ordinary surface plasmon in Ref. [36]. This allows us to solve the dispersion of surface CBP in the hydrodynamic approximation and find that the interband transitions will compete with the AHC in affecting the surface CBP. In addition, we include the intrinsic AHC calculated from the density functional theory (DFT), whose tensor form modifies the properties of the surface CBP. Now we have two modes for long wavelength surface CBP instead of one as predicted by ZV.

The paper is organized as follows. We will work on the collisionless hydrodynamic approximation to determine the effects of the interband transitions and the AHC tensor on the surface CBP plasmons. Section II discusses the applicable conditions of this approximation, the semiclassical treatment of the intrinsic AHC (Sec. II A) and the  $s$ - $d$  polarization model for considering the interband transitions (Sec. II B). Section II C introduces the process to obtain the implicit dispersion relation Eq. (23). Section III contains the computational methods for calculating the band structure and the interband transitions of the disordered bulk Py. All the numerical results are presented in Sec. IV. Beginning with the electronic (Sec. IV A) and optical properties (Sec. IV B) obtained from the DFT calculations, we explain the necessary of including interband transitions in solving the dispersion of surface CBP on the Py. Then the effects of the interband transitions, the AHC and the direction of wave vector with respect to the magnetization on the dispersion are discussed in Sec. IV C. Finally, in Sec. V, we summarize our main findings and outlook their potential applications.

## II. HYDRODYNAMIC THEORIES

Surface plasmon stands for the oscillation of charge density in the interface region. To begin with, we treat the Py as a semi-infinite electron gas occupying the space  $z < 0$ . When neglecting retardation, that is all interactions are taken to be

instantaneous, the surface plasmon is entirely longitudinal. This is quite a good approximation as long as we are concerned with the plasmons whose parallel wave vectors satisfy  $|q_{\parallel}| > \omega/c$ . In the retarded region, one should go beyond the electrostatic limit and consider the full set of Maxwell's equations, so that surface plasmon will interact with the electromagnetic radiation and form the surface-plasmon polariton.

To focus on the long wavelength surface plasmon mode, we do not deal with the spatial variation of the equilibrium electron density in the surface region, considering its relatively short decay length, instead we assume a uniform electronic density profile abruptly terminated at the interface, that is the equilibrium density  $n_0(\mathbf{r}, \omega) = n_0\Theta(-z)$  with  $\Theta$  being the Heaviside step function. For a longitudinal density wave, the induced density,  $n_1(\mathbf{r}, \omega)$ , has a dipolar form and associates with the electric field by Gauss's law,

$$\nabla \cdot \mathbf{E}(\mathbf{r}, \omega) = -en_1(\mathbf{r}, \omega)/\epsilon_0. \quad (1)$$

Then the dynamics of the density fluctuation can be understood from the hydrodynamic model with the continuity equation

$$\partial_t n_1 + \nabla_{\mathbf{r}} \cdot \mathbf{j} = 0 \quad (2)$$

and the Euler equation

$$\partial_t \mathbf{j}_p + s^2 \nabla_{\mathbf{r}} n_1 - \frac{en_0}{m} \nabla_{\mathbf{r}} \varphi = 0, \quad (3)$$

where  $m$  is the dynamical mass characterizing the collective motion of the Fermi sea. The electron gas has been treated as compressible fluid ignoring shear force and viscous force as mentioned in Ref. [35].  $s$  is the speed of the compressional wave, which has the same order of Fermi velocity.  $\mathbf{j}$  is the physical current density given by  $\mathbf{j} \equiv \mathbf{j}_p + \mathbf{j}_A$ , where  $\mathbf{j}_p = n_0 \langle -i\hbar \nabla_{\mathbf{k}} \rangle / m$ , averaging over the Bloch wave function, is the canonical current density, while  $\mathbf{j}_A$  is the current density resulting from the field momentum, which in Py is the anomalous velocity due to the Berry curvature of the band structure in the absence of external electromagnetic fields.

The essential idea of the proper hydrodynamic approximation is that the relaxation of system to thermodynamic equilibrium is so fast that "local equilibrium" is always maintained. However, it is not the case for plasmons in the electron liquid, where the restoring force is primarily provided by the long-range Coulomb interaction. At long wavelength the frequency associated with this restoring force corresponds to the plasmon frequency, which is much larger than the inverse of electron relaxation time. Consequently, the system is considered to be in the collisionless regime. For disordered Py,  $\tau \sim 0.1$  ps [37,38] and the surface plasmon frequency is about 1.9 eV according to our DFT calculations, which allows us to employ the collisionless hydrodynamic approximation to effectively model the behavior of surface plasmons on Py. Another factor that will affect the validity of this approximation is that the collective surface modes may couple to electron-hole pair excitations. However, this coupling can be neglected in the long wavelength limit with wave vectors  $q < q_c \approx \omega_p/v_F$ .

### A. The anomalous velocity

The anomalous velocity can be understood well based on the quasiclassical equations of motion of the electron wave packets, as explained in the review paper [39]. We restate the key conclusions here to keep the integrity of our model:

$$\dot{\mathbf{r}} = \frac{1}{\hbar} \frac{\partial \epsilon_M(\mathbf{k})}{\partial \mathbf{k}} + \boldsymbol{\Omega}_n(\mathbf{k}) \times \dot{\mathbf{k}}, \quad (4)$$

$$\hbar \dot{\mathbf{k}} = -e\mathbf{E} - e\dot{\mathbf{r}} \times \mathbf{B}, \quad (5)$$

with  $\epsilon_M(\mathbf{k}) = \epsilon_n(\mathbf{k}) - \mathbf{M} \cdot \mathbf{B}$ . In the absence of magnetic fields, Eqs. (4) and (5) are the same as the traditional Bloch electron equations of motion except for an additional term proportional to the Berry curvature, namely the anomalous velocity,

$$\mathbf{v}_{a,n}(\mathbf{k}) \equiv \boldsymbol{\Omega}_n(\mathbf{k}) \times \dot{\mathbf{k}}, \quad (6)$$

reflecting the nonconservation of Bloch momentum in physics.  $\boldsymbol{\Omega}_n(\mathbf{k})$  represents Berry curvature,

$$\boldsymbol{\Omega}_n(\mathbf{k}) = \nabla_{\mathbf{k}} \times \langle u_n(\mathbf{k}) | i \nabla_{\mathbf{k}} | u_n(\mathbf{k}) \rangle, \quad (7)$$

where  $u_n(\mathbf{k})$  is the periodic part of the Bloch function with  $n$  being the band index.

The presence of the anomalous velocity leads to the intrinsic AHC, which can be derived from the drift of equilibrium distribution in pure magnetic crystal without considering any scattering processes [40]. In the absence of magnetic fields, the electrical current density caused by the equilibrium distribution function  $f_n(\mathbf{k})$  becomes

$$\begin{aligned} \mathbf{j}_e &= \frac{-e}{(2\pi)^3} \sum_n \int_{BZ} f_n(\mathbf{k}) \dot{\mathbf{r}}(\mathbf{k}) d^3k \\ &= \boldsymbol{\sigma}_{\text{AHC}} \times \mathbf{E}, \end{aligned} \quad (8)$$

with

$$\boldsymbol{\sigma}_{\text{AHC}} = \frac{e^2}{(2\pi)^3 \hbar} \sum_n \int_{BZ} f(\mathbf{k}) \boldsymbol{\Omega}_n(\mathbf{k}) d^3k \quad (9)$$

being the intrinsic AHC. The total physical current density then becomes

$$\mathbf{j} \equiv \mathbf{j}_p + \frac{\boldsymbol{\sigma}_{\text{AHC}} \times \mathbf{E}}{-e}. \quad (10)$$

It is worth noting that the AHC will not affect the bulk plasmon mode in that it will not change the hydrodynamic equations (2) and (3): the anomalous velocity is perpendicular to both of the electric field and the spatial gradient so that only  $\mathbf{j}_p$  contributes to the time derivative in the Euler equation and the continuity equation is also unchanged. However, the AHC will manifest itself in the boundary conditions and therefore affect the surface plasmons as we will see in Sec. II C. This point was clearly demonstrated by SR [21] for the edge plasmon of a 2D system and by ZV [35] for the surface plasmon of a 3D system.

### B. The effect of interband transitions

In general, interband transitions take place at frequency far larger than the bulk plasmon, so that their contribution to the dielectric function near plasmon frequency can be negligible. But for some metals, such as Au and Ag, their

interband transitions can be excited by the electromagnetic wave of frequency less than that of the bulk plasmon. For Py, according to our DFT calculations, the onset frequency of interband transition, at about 1.2 eV, lies only slightly below the surface plasmon frequency from the Drude model,  $\omega_s(q=0) = \omega_p/\sqrt{2} = 1.9$  eV. Therefore there will be strong mutual influence between the bulk interband transitions and the collective surface excitations. And the dynamical dielectric function must be taken into account in the model even though the surface CBP is a self-sustained eigenmode with no incident light being employed.

The electrostatic potential  $\varphi$ , which is assumed to be instantaneously created by the charge density according to the modified Poisson equation

$$\epsilon_d \nabla_r^2 \varphi = \frac{en_1}{\epsilon_0}, \quad (11)$$

where  $\epsilon_0$  is the vacuum permittivity and  $\epsilon_d$  the interband dielectric function. Strictly speaking,  $\epsilon_d$  should be a tensor and a function of  $\omega$  as we use in calculating the dispersions in Sec. II C. We treat it as a scalar in Eq. (11) to simplify the explanation of the  $s$ - $d$  polarization model [36]. Here  $s$  refers to the electrons that occur intraband transitions, and  $d$  to those that occur interband transitions. From Gauss's law, we have

$$\nabla \cdot \mathbf{E} = -\frac{e(n_1 + n_d)}{\epsilon_0}, \quad (12)$$

where  $n_d$  stands for the polarization-charge density due to interband transitions. By introducing the polarization such that  $\nabla \cdot \mathbf{P}_d = en_d$ , it is easy to see the interband dielectric function appears in Gauss's law as

$$\epsilon_d \nabla \cdot \mathbf{E} = -\frac{en_1}{\epsilon_0} \quad (13)$$

by noting that  $\epsilon_d \mathbf{E} = \mathbf{E} + \mathbf{P}_d/\epsilon_0$ , so that the Poisson equation is modified to be Eq. (11).

### C. Dispersion relation of the surface CBP

As discussed in Sec. II A, without the confinement of boundary conditions, the AHC does not take effect in the hydrodynamic equations, which leaves the dispersion of bulk plasmons unaffected by the anomalous velocity. However, for the solution of surface plasmon mode, the AHC does have an impact on the current density normal to the interface. Considering a semi-infinite metal as shown in Fig. 1(b), the electric potential is continuous due to  $E_{\parallel}|_{z=0^-} = E_{\parallel}|_{z=0^+}$ , while the continuity of its derivative is not true in general except for accompany with the vanishing current density outside the metal, which results from  $D_{\perp}|_{z=0^-} = D_{\perp}|_{z=0^+}$ . In the presence of interband transitions, the correct form of the electrical current density consists of two parts, the normal charge current density and the polarization current density, such that its perpendicular component should be  $j_e^z = -ej_z + \frac{dP_z}{dt}$ , where  $j_z$  is the  $z$ -component of the physical current density that includes the AHC as shown in Eq. (10). In the frequency domain, the electrical current density becomes

$$j_e^z(\omega) = -ej_z(\omega) + [\epsilon_d(\omega) - 1]i\omega\epsilon_0\partial_z\varphi(\omega). \quad (14)$$

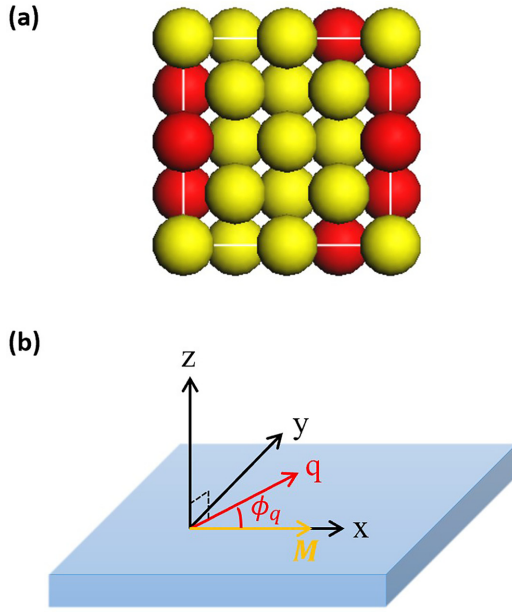


FIG. 1. Crystal structure and the coordinates system of Py. (a) The  $2 \times 2 \times 2$  supercell of fcc disordered Py. Red (yellow) spheres represent Fe (Ni) atoms. The lattice constant is  $3.537 \text{ \AA}$ . (b) Schematics of semi-infinite 3D Py: the magnetization is in-plane along  $x$  axis.  $\mathbf{q}$  is the wave vector of surface plasmon, which is in the  $x$ - $y$  plane at an angle  $\phi_q$  with respect to the magnetization.

Therefore the full boundary conditions should include

$$\varphi|_{z=0^-} = \varphi|_{z=0^+}, \quad (15)$$

$$\partial_z \varphi|_{z=0^-} = \epsilon_1 \partial_z \varphi|_{z=0^+}, \quad j_z^z|_{z=0^-} = 0, \quad (16)$$

where  $\epsilon_1$  denotes the dielectric constant of the medium outside the metal.

Given the uniform distribution of the equilibrium electron within the metal and the longitudinal characteristic of the surface plasmon mode, the Fermi liquid under discussion is translationally invariant parallel to the surface. This allows us to assume all the physical quantities, such as  $n_1$ ,  $\mathbf{j}_p$  and  $\varphi$ , take the form of  $e^{\kappa z} e^{i(\mathbf{q}\mathbf{r} - \omega t)}$ , with  $\mathbf{q}$  and  $\mathbf{r}$  in the  $x$ - $y$  plane and  $\kappa > 0$ . Substituting these ansatz into the hydrodynamic equations (2) and (3) and the modified Poisson equation (11), we obtain an eigenproblem for the undetermined amplitudes of  $n_1$  and  $\mathbf{j}_p$ , such that

$$\begin{pmatrix} 0 & \mathbf{Q} \\ \alpha \mathbf{Q}^T & 0 \end{pmatrix} \begin{pmatrix} n_1 \\ \mathbf{j} \end{pmatrix} = i\omega \begin{pmatrix} n_1 \\ \mathbf{j} \end{pmatrix}, \quad (17)$$

where  $\mathbf{Q} = (iq_x, iq_y, \kappa)$  and

$$\alpha = s^2 - \frac{1}{\epsilon_d} \frac{\omega_p^2}{\kappa^2 - q^2} \quad (18)$$

with  $q = |\mathbf{q}|$  and  $\omega_p^2 = e^2 n_0 / (\epsilon_0 m)$  being the bulk plasmon frequency from the Drude model. Its eigenvalue gives the relation of  $\kappa$  and  $q$

$$\kappa^2 = q^2 + s^{-2} (\omega_p^2 / \epsilon_d - \omega^2). \quad (19)$$

Evidently,  $\kappa$  depends explicitly on both  $q$  and  $\omega$ . Equation (19) has two types of solutions: one is  $\kappa = \pm q$ , corresponding to

the solution when no electron density is induced; the other one is  $\kappa \neq \pm q$ , for  $n_1 \neq 0$ . We can write down the general solution for the electrostatic potential as

$$\varphi = \varphi_1 e^{\kappa z} e^{i\mathbf{q}\cdot\mathbf{r}} + \varphi_2 e^{-qz} e^{i\mathbf{q}\cdot\mathbf{r}}, \quad z < 0 \quad (20)$$

$$\varphi = \varphi_0 e^{-qz} e^{i\mathbf{q}\cdot\mathbf{r}}, \quad z > 0 \quad (21)$$

and that for the density oscillation, which is according to the Poisson equation (11),

$$n_1 = \frac{(\kappa^2 - q^2) \epsilon_0 \epsilon_d}{e} \varphi_1 e^{\kappa z} e^{i\mathbf{q}\cdot\mathbf{r}}, \quad (22)$$

with  $\varphi_1$ ,  $\varphi_2$ , and  $\varphi_0$  being integration constants to be determined by the boundary conditions, and  $\kappa, q > 0$ . The time-dependent part  $e^{-i\omega t}$  has been suppressed for clarity. Applying the boundary conditions (15) and (16), we obtain a set of linear equations for the amplitudes  $\varphi_i$  ( $i = 0, 1, 2$ ), whose secular equation gives the dispersion relation of the surface CBP,

$$\begin{aligned} & \omega^2 \epsilon_0 [\kappa(\epsilon_1 + \epsilon_d) + q\epsilon_1(\epsilon_d - 1)] - \omega_p^2 \epsilon_0 (\kappa + q\epsilon_1) \\ & + \omega(q - \kappa)(\sigma_{zx} \cos \phi_q + \sigma_{zy} \sin \phi_q) = 0, \end{aligned} \quad (23)$$

where  $\sigma_{\alpha\beta}$  ( $\alpha, \beta = x, y, z$ ) is the tensor form of the AHC [41] such that  $\mathbf{j} = \mathbf{j}_p + \overleftarrow{\boldsymbol{\sigma}} \cdot \mathbf{E} / (-e)$ ,  $\phi_q$  is the angle between the wave vector of surface plasmon and the magnetization. It is called Berry plasmon because its dispersion depends on the Berry curvature of band structure. The chirality will be discussed as below.

It is instructive to first examine the solutions in the long wavelength limit ( $q \rightarrow 0$ ) for which Eq. (23) reduces to

$$\omega^2 \epsilon_0 (\epsilon_1 + \epsilon_d) - \omega_p^2 \epsilon_0 - \omega(\sigma_{zx} \cos \phi_q + \sigma_{zy} \sin \phi_q) = 0, \quad (24)$$

which has two possible solutions,

$$\begin{aligned} \omega_{\pm} = & \frac{(\sigma_{zx} \cos \phi_q + \sigma_{zy} \sin \phi_q)}{2\epsilon_0(\epsilon_1 + \epsilon_d)} \\ & \pm \frac{\sqrt{(\sigma_{zx} \cos \phi_q + \sigma_{zy} \sin \phi_q)^2 + 4\epsilon_0^2 \omega_p^2 (\epsilon_1 + \epsilon_d)}}{2\epsilon_0(\epsilon_1 + \epsilon_d)}. \end{aligned} \quad (25)$$

Unlike in normal definitions, we have enforced  $q$  to be positive and thus  $\omega$  can be either positive or negative, whose sign indicates the propagation direction of the surface mode. When  $\sigma_{\alpha\beta} \rightarrow 0$ , the solution becomes  $|\omega| = \omega_p / \sqrt{\epsilon_1 + \epsilon_d}$ , reproducing the 3D surface plasmon frequency at  $q = 0$ . The effect of interband transition should not be ignored for metals like Py, even if  $\sigma_{\alpha\beta} = 0$  as discussed in Secs. IV A and IV B. For  $\sigma_{\alpha\beta} \neq 0$ , the two solutions represent two modes of surface plasmon since  $\omega_+(-\phi_q) \neq -\omega_- (\phi_q)$  except for  $\phi_q = \pi/2$  or  $\sigma_{zx} = 0$ , indicating that the chirality of surface Berry plasmons is indeed resulting from the AHC, or in other words, from the Berry curvature of the Py's band structure.

Moreover, it should be aware of that  $\epsilon_d$  could be a nonlocal dynamic dielectric function, i.e., a function of both  $q$  and  $\omega$ , which requires solving Eq. (25) further to get the final solutions. In contrast, as  $\sigma_{\alpha\beta} = 0$  and  $\epsilon_1 = \epsilon_d = 1$ , Eq. (23)

gives the analytical expression of the ordinary surface plasmon dispersion,

$$\omega_{\pm} = \pm \frac{1}{2} \left( \sqrt{2\omega_p^2 + q^2 s^2} + qs \right). \quad (26)$$

Since  $\omega_+ = -\omega_-$ , the two solutions represent the same surface plasmon mode but propagating in opposite directions. Hence, ordinary surface plasmons do not possess any chirality.

### III. COMPUTATION METHODS AND DETAILS

#### A. Special quasirandom structure

A standard supercell approach to model disordered alloys involves a randomly generated impurity distribution within the alloy matrix, which always renders a huge supercell that is unfeasible for DFT calculations. To model disordered Py in a finite supercell, we employed the Alloy Theoretic Automatic Toolkit (ATAT) [42] within the framework of Special Quasirandom Structures (SQSs) generated by the Monte Carlo annealing loop algorithm [43]. Alternative approximations include the coherent potential approximation (CPA) and the cluster expansion (CE) method. There are two advantages of SQS: one is that it can perfectly match the maximum number of correlation functions of the supercell to those of a random alloy; the other is that it is computationally less demanding.

We constructed a 32-atom SQS for the disordered  $\text{Ni}_{80}\text{Fe}_{20}$  (with 26 Ni atoms and 6 Fe atoms). Although the SQS approach allows an arbitrary supercell size and shape ( $A \times B \times C$ ) in terms of lattice vectors to achieve the best randomness, we have traded off the shape freedom and chosen ( $A \times A \times A$ ) to ensure our model preserve the point group symmetry that Py shows experimentally. However, the size effect on the performance of SQS to describe optical properties has not been studied systematically. We, therefore, use the same size of supercell ( $2 \times 2 \times 2$ ) as has been checked by Zhang *et al.* for fcc Fe-Ni-Cr disordered alloys [44]. The optimized crystal structure is fcc as shown in Fig. 1, where the red (yellow) spheres represent iron (nickle) atoms with a lattice constant of 3.537 Å, which is very close to the experimental values [45–47].

#### B. First-principles calculations of electronic and optical properties

To get a quantitative prediction of the surface CBP on the disordered Py, we performed the first-principle calculations using the Vienna *ab initio* simulation package (VASP) [48] in combination with the crystal structure predicted by ATAT. Both spin-polarized and self-consistent relativistic band structures were carried out with the projector-augmented-wave (PAW) method [49], and a kinetic-energy cutoff of 500 eV was used for the plane-wave basis. We have chosen the Perdew-Burke-Ernzerhof (PBE)-type [50] generalized gradient approximation (GGA) [51] for the exchange-correlation functional. The valence electron configurations of Fe and Ni elements used in PAW potentials were  $3d^7 4s^1$  and  $3d^9 4s^1$ , respectively. A  $4 \times 4 \times 4$  Gamma-grid [52,53] containing  $\Gamma$  and other high-symmetry points was applied to sample the full BZ, so that the band extrema are typically included in

the calculation of dielectric function. The lattice constants and atom coordinates were optimized with total energy convergence criterion less than  $10^{-5}$  eV/cell and force less than 0.02 eV/atom.

We then employed the WANNIER90 [54] interface combined with WANNIERTOOLS [55] to calculate the Berry curvature and the AHC, which has great significance for the dispersion. The AHC was calculated by means of the Wannier interpolation [41] to avoid the usage of a dense  $k$  mesh, as implemented in the WANNIER90 package. The starting projection for constructing maximally localized Wannier function were chosen as  $d$  orbitals of Fe and  $d$  orbitals of Ni. The upper bound for the inner and outer window for the band disentanglement procedure were chosen at  $-5$  and  $15$  eV to the Fermi level.

Finally, We calculated the complex interband dielectric function with the built-in function in VASP in the random-phase approximation (RPA) including local field corrections. This can be done using the standard longitudinal expression of the dielectric tensor [53]. The imaginary part of interband dielectric function is given by

$$\epsilon_{\alpha\beta}^{(2)}(\omega) = \frac{8\pi^2 e^2}{\Omega} \lim_{q \rightarrow 0} \frac{1}{q^2} \sum_{o,u,k} w_k \delta(E_{u,k} - E_{o,k} - \omega) \times \langle u_{u,k+\hat{e}_\alpha q} | u_{o,k} \rangle \langle u_{u,k+\hat{e}_\beta q} | u_{o,k} \rangle^*, \quad (27)$$

where  $\hat{e}$  and  $q$  stand for the polarization and the wave vector of incident light, respectively.  $w_k$  denote the  $k$ -point weights. Only direct transitions from occupied (labeled by  $o$ ) and unoccupied ( $u$ ) Kohn-Sham states are taking into account.  $\alpha$  and  $\beta$  refer to Cartesian coordinates and  $\Omega$  the volume of the unit cell. BZ integrations were performed using a Gaussian smearing method with a width of 0.2 eV. To simplify our discussion on the obtained dielectric function in Sec. IV B, we also give the transversal expression although unused in our calculations,

$$\epsilon_{\alpha\beta}^{(2)}(\omega) = \frac{4\pi^2 e^2 \hbar^4}{\Omega \omega^2 m_e^2} \lim_{q \rightarrow 0} \sum_{o,u,k} 2w_k |P_{ou}|_{\alpha\beta}^2 \times \delta(E_{u,k} - E_{o,k} - \omega) \quad (28)$$

with the transition matrix

$$|P_{ou}|_{\alpha\beta}^2 = \langle u_{u,k} | i\nabla_\alpha - \mathbf{k}_\alpha | u_{o,k} \rangle \langle u_{u,k} | i\nabla_\beta - \mathbf{k}_\beta | u_{o,k} \rangle^*. \quad (29)$$

The real part of the interband dielectric function  $\epsilon_{\alpha\beta}^{(1)}(\omega)$  is obtained from the imaginary part  $\epsilon_{\alpha\beta}^{(2)}(\omega)$  by the usual Kramers-Kronig transformation,

$$\epsilon_{\alpha\beta}^{(1)}(\omega) = 1 + \frac{2}{\pi} P \int_0^\infty \frac{\epsilon_{\alpha\beta}^{(2)}(\omega') \omega'}{\omega'^2 - \omega^2 + i\eta} d\omega', \quad (30)$$

where  $P$  stands for the principal value and  $\eta$  is the complex shift parameter, which was set to be 0.1 in the calculation.

## IV. RESULTS AND DISCUSSION

### A. Electronic properties of Py

Figure 2 shows the band structures and the density of states (DOS) of the Py with (a) and without (b) spin-orbit coupling (SOC) calculated from the VASP. It can be seen that the Py has no band gap and is spin polarized [Fig. 2(a)] near the

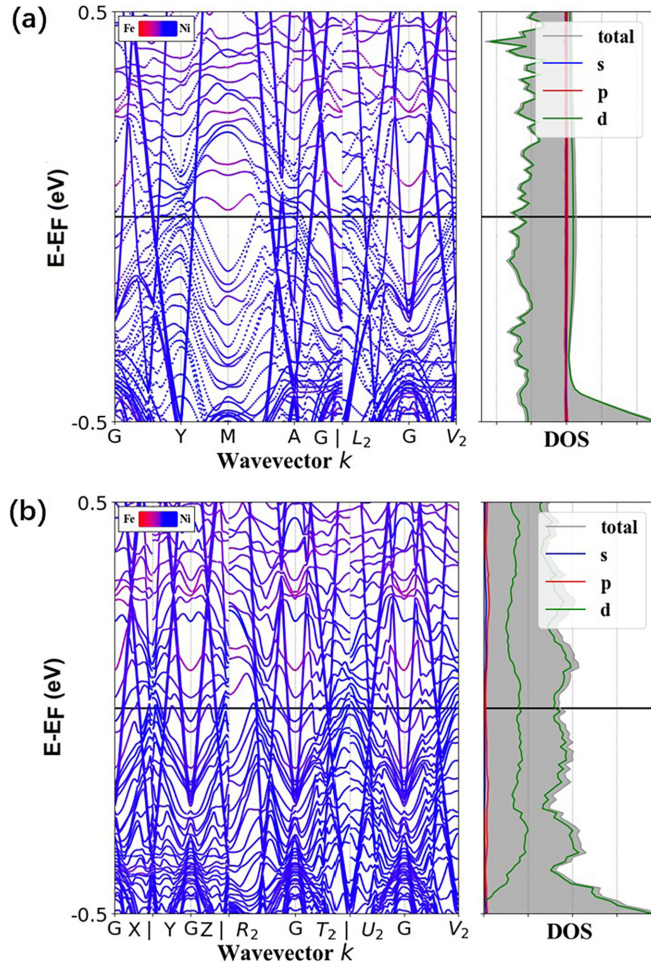


FIG. 2. Band structures and densities of states of Py: (a) without spin-orbit coupling, the solid lines represent the spin-up result and the dashed lines the spin-down result; (b) with spin-orbit coupling.

Fermi surface, indicating that the calculated Py is indeed a ferromagnetic metal. As shown in Fig. 2(b), the presence of SOC does not change the Py's metallic characteristics and the  $3d$  electrons of Ni and Fe atoms play a major role near the Fermi surface, which suggests the interband transitions may affect the overall frequency of the surface plasmon as observed on Ag [36]. If the onset frequency of the interband transitions is below  $\omega_p/\sqrt{2}$ , then it is a strong evidence that we should consider the dynamic dielectric function of the bulk Py. Moreover, the obtained total magnetic moment with considering SOC is  $31.42 \mu_B$ , corresponding to a magnetization of  $8.23 \times 10^5 \text{ A m}^{-1}$ , in agreement with the experimental results [45].

### B. Interband transitions of Py

Interband transitions can be studied by calculating the dynamic dielectric function within the VASP. The peaks in the imaginary part of the dielectric function ( $\text{Im}[\epsilon(\omega)]$ ) reveal the prominent transitions. As shown in Fig. 3, the local field correction (LFC) [56,57] is important in the presence of SOC, without which transitions below the bulk plasma frequency (peaks on the left of the dashed line) might be missing.

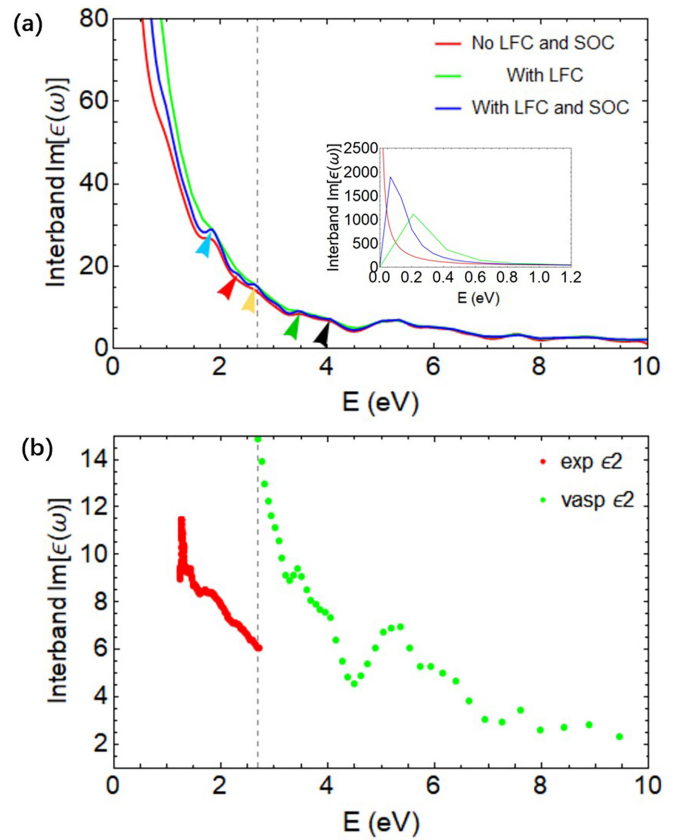


FIG. 3. The imaginary parts of interband dielectric functions of Py. The effects of the local field correction (LFC) and the spin-orbit coupling (SOC) on  $\epsilon_{yy}$  have been compared in (a). The inset shows more details in the long wavelength limit. The vertical dashed line marks the bulk plasma frequency,  $\omega_p^2 = 7.311 \text{ eV}^2$ . (b) compares the result from VASP calculations with that from experiments [58].

Besides, the inset shows that LFC should be taken into account even if in the absence of SOC. Although LFC is independent of frequency, it will resolve the divergence of  $\text{Im}[\epsilon(\omega)]$  as  $\omega \rightarrow 0$ .

To understand the main features of the dielectric function, we plot the projected density of states (PDOS) of the Py in Fig. 4. As already shown in Fig. 2(b), the bands near Fermi level are dominated by Fe- $d$  and Ni- $d$  orbitals. The selection rule of dipole transitions also requires analysis of DOSs projected on the other orbitals. Above the Fermi level, the structure is mainly determined by the  $d$  orbitals of Fe and Ni, while below the Fermi level, the states have a mixed characteristic of  $p$  and  $d$  orbitals. According to the peak positions in the PDOS and the selection rule of dipole transitions, there might be interband transitions from  $s$  to  $p$  orbitals, from  $sp$  hybridization orbitals to  $d$  orbitals, as well as between  $p$  and  $d$  orbitals of Fe and Ni atoms. We have labeled the prominent transition peaks around the bulk plasmon frequency with arrows of different colors in Fig. 3. The corresponding occupied and unoccupied states are marked by arrows of the same color in Fig. 4. The blue arrow, for example, at about 1.8 eV in Fig. 3 corresponds to the blue arrows in Fig. 4 for the  $p$ - $d$  transition.

Next, to determine whether interband transitions are crucial in our study on the surface CBP, we have to identify the onset

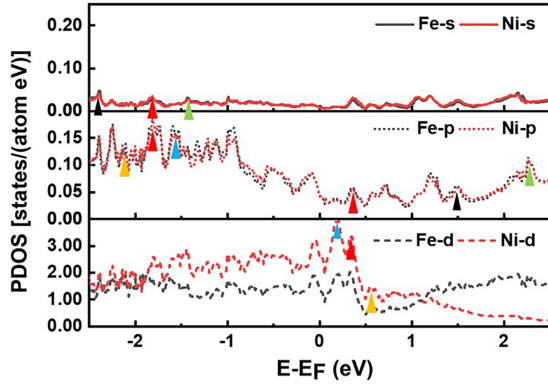


FIG. 4. Projected density of states (PDOS) of  $s$ ,  $p$  and  $d$  orbitals of Fe and Ni atoms in Py with local field correction and spin-orbit coupling. The black (red) lines are the results of Fe (Ni) atoms.

frequency of the transitions. Normally, this can be done by searching for intersects with the horizontal axis or the absorption edge in the figure of  $\text{Im}[\epsilon(\omega)]$ . However, there exists a huge peak below 1 eV arising from  $d$ - $d$  transitions as shown in Fig. 3, which smears off the absorption edge in our calculation. Although such a transition should be suppressed by the selection rule, it acquires some strength due to hybridization with the surrounding atoms. A small but finite  $d$ - $d$  transition matrix element when divided by  $\omega^2$  as in Eq. (28) yields the blowup in the low-energy part of  $\text{Im}[\epsilon(\omega)]$ , which leads to a larger  $\text{Im}[\epsilon(\omega)]$  than the experimental result [58] as shown in Fig. 3(b). This calculation flaw has also been discussed in the DFT study of Mg-Ti alloys [59]. Nevertheless, one can estimate the onset frequency from the PDOS (Fig. 4) to be about 1.2 eV due to  $p$ - $d$  transition, which also agrees well with the experimental absorption edge as shown in the red curve in Fig. 3(b). This onset frequency lies slightly below the surface plasmon frequency of Py,  $\omega_p/\sqrt{2} = 1.9$  eV, and therefore, the interband transitions will have a strong effect on the surface plasmon dispersion.

The finite  $d$ - $d$  transition also affects badly on the accuracy of  $\text{Re}[\epsilon(\omega)]$ . According to Eq. (30), the larger  $\text{Im}[\epsilon(\omega)]$  is in the low-energy region, the more likely  $\text{Re}[\epsilon(\omega)]$  becomes negative. To illustrate the impact, we compare the real parts of the dielectric functions calculated from experiments [58], the Drude model (i.e., the intraband transitions) and the VASP (i.e., the interband transitions) in Fig. 5. To make a direct comparison between the interband dielectric function obtained through VASP calculation and that from the experiments, we have subtracted the Drude contribution ( $-\omega_p^2/\omega^2$ ) from the experimental result in Fig. 5(b). The results show a large discrepancy between the two as expected, but the interband transitions do contribute to the dynamic dielectric function in the range between  $\omega_p/\sqrt{2}$  and  $\omega_p$  [red curve in Fig. 5(b)]. Therefore we should consider the bulk dielectric function of Py in the study of CBP propagating on the surface of Py.

### C. Dispersion of surface CBP on Py

The key result of this work is Eq. (23), through which one can get the dispersion of surface CBP on any bulk magnetic metals for given AHC and dynamic bulk dielectric function.

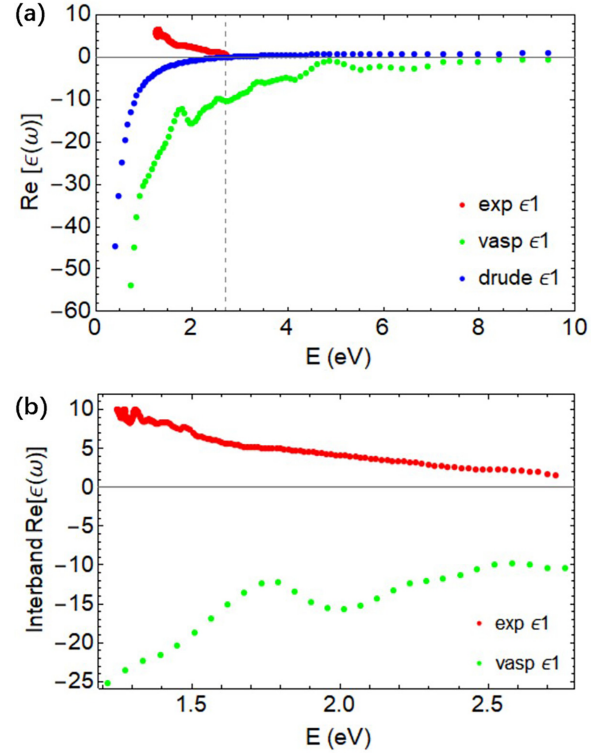


FIG. 5. The real parts of dielectric functions. (a) Comparison of the results from experiments [58], the DFT calculations and the Drude model. The light gray dashed line locates the position of the bulk plasma frequency,  $\omega_p^2 = 7.311$  eV<sup>2</sup>. (b) The real parts of the interband dielectric functions from the experiments and the DFT calculation.

Here we assume the bulk Py is placed in vacuum and use the results from our DFT calculations and previous experiments [58,60,61] to give a qualitative understanding of the dispersion. Magnitudes of wave vectors  $q$  have been taken to be less than  $q_c \approx \hbar\omega_p k_F / (2E_F)$  to ensure the validity of the hydrodynamic approximation. According to our DFT calculations,  $\omega_p = 2.704$  eV,  $E_F = 8.686$  eV, so that we keep the dispersion with positive  $q$  less than  $0.16 k_F$  only.

In Sec. II C, we have discussed the chirality of the surface Berry plasmon as  $q \rightarrow 0$ . The dispersions of surface CPB with finite  $q$  are shown in Figs. 6–8. The figures are plotted for the surface CPB propagating in the direction perpendicular to the magnetization ( $\phi_q = \pi/2$ ), and therefore, only  $\sigma_{zy}$  takes effect. The nonzero AHC is the intrinsic one calculated from the VASP in Figs. 6 and 7.

As discussed in previous sections, both the AHC and the interband transitions take effect on the surface plasmons on the disordered Py. To understand better the qualitative difference of the two effects, we will check the impact of AHC alone first in Fig. 6. The dashed line is the dispersion of ordinary surface plasmon calculated from Eq. (26), which is symmetric about  $\omega = 0$ . A nonzero AHC breaks the symmetry and shifts the dispersion upward, making the ordinary surface plasmon mode split into two chiral modes, which are the so-called surface CBPs. For a given  $q$ , these two modes propagate in the opposite directions but have different phase

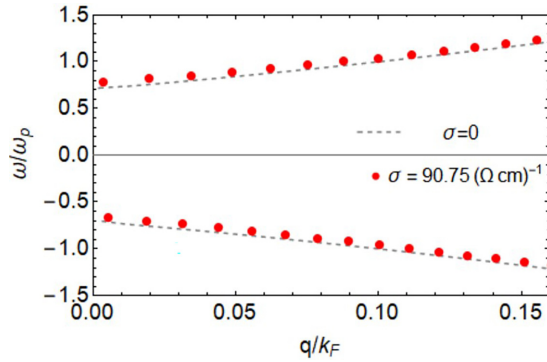


FIG. 6. The effect of the AHC on the surface plasmon dispersion with  $\epsilon_d = 1$  (i.e., without interband transitions),  $\phi_q = \pi/2$ ,  $s^2 = 2.6 \times 10^{12} \text{ m}^2 \text{ s}^{-2}$ ,  $\omega_p^2 = 7.311 \text{ eV}^2$ , and  $\sigma_{zy} = 90.75 (\Omega \text{ cm})^{-1}$ . The dashed line is the analytical solution calculated from Eq. (26).

velocity and therefore cannot produce a standing wave by a linear combination.

In Fig. 7, we study the effects of both the AHC and the interband transitions on the surface plasmon dispersion of the Py. The interband transition manifests itself as a nonlocal dielectric function  $\epsilon_d(z, z', q, \omega)$  in the model. For small  $q$  and far from the surface, a local dielectric function  $\epsilon_d(\omega)$  should be good enough to approximate its effect. As discussed in Sec. IV B, there is a flaw in the DFT calculation due to a fictive  $d$ - $d$  transition shown in Fig. 3, hence we have used the experimental results to deal with  $\epsilon_d$ , which is the same as interband  $\text{Re}[\epsilon(\omega)]$  [the red curve in Fig. 5(b)]. Since the interband dielectric function extracted from the experiments does not cover the full range of the surface plasmon frequency, we have to approximate it as some positive constant here considering it varies slowly between 2 to 12 with changing  $\omega$ . The larger the  $\epsilon_d$ , the stronger the interband transition is.  $\epsilon_d = 1$  corresponds to the case without considering interband transitions. There exhibits two tendencies as increasing  $\epsilon_d$ ,

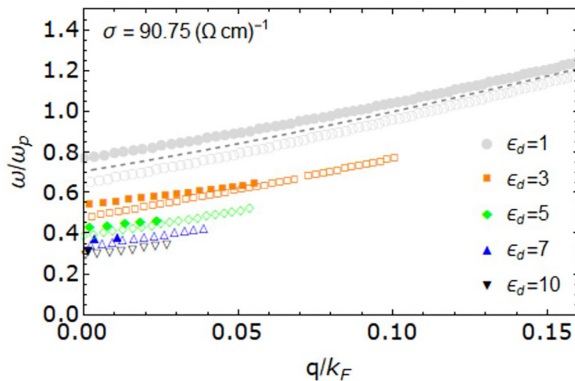


FIG. 7. The effect of interband transitions on the surface CBP dispersion with  $\phi_q = \pi/2$ ,  $s^2 = 2.6 \times 10^{12} \text{ m}^2 \text{ s}^{-2}$ ,  $\omega_p^2 = 7.311 \text{ eV}^2$ , and  $\sigma_{zy} = 90.75 (\Omega \text{ cm})^{-1}$ . The dashed line is the analytical solution calculated from Eq. (26). The filled points stands for the forward propagating modes ( $\omega_+$ ), while the hollow points stands for the backward propagating modes ( $\omega_-$ ). We have taken absolute values for the frequencies to compare the frequency differences of the two modes.

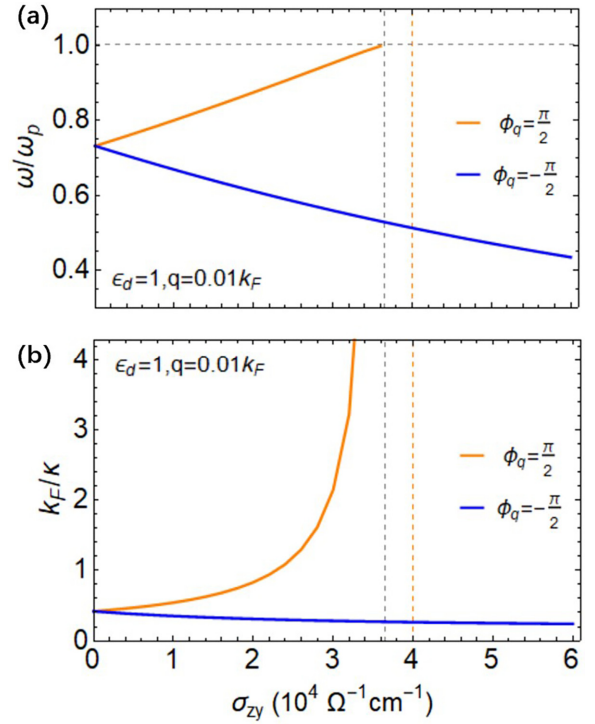


FIG. 8. The frequency (a) and the decay length (b) as a function of  $\sigma_{zy}$  at  $q = 0.01 k_F$ . The gray dashed lines denote the cutoff frequency and the corresponding threshold AHC. The orange dotted line denotes the AHC chosen in Fig. 9.

one is the overall decrease of the surface CBP frequency and splitting of the two modes, the other is the disappearance of surface modes, which can be understood well from Eq. (19) such that  $\kappa$  becomes pure imaginary as  $\epsilon_d$  goes to infinity. For certain range of  $q$ , there is only one chiral mode left, indicating its potential application on technologies that rely on nonreciprocity.

The disappearing of the forward propagating mode can also be achieved with increasing the AHC. Figures 6 and 7 are based on the intrinsic AHC due to the Berry curvature of band structure. However, in disordered ferromagnetic metals, the extrinsic mechanisms such as side-jump and skew scattering may play an even more important role in producing AHC, which results in a much larger AHC and even a change of sign [60,61]. We thus depict the effect of increasing AHC on the two chiral modes in Fig. 8. To avoid the competitive effect of interband transitions we have let  $\epsilon_d = 1$ . The negative mode has been taken as absolute value and denoted by  $\phi_q = -\pi/2$ . In contrast to the effect of  $\epsilon_d$ , increasing AHC will not only eliminate one chiral mode for certain  $q$ , but also enlarges the overall frequency and the frequency difference between the two chiral modes, as shown in Fig. 8(a). Above a threshold value of AHC, the forward propagating mode merges with the bulk mode, which is apparent as a divergence of the decay length in Fig. 8(b).

The dependence of surface CBP frequency on  $\phi_q$  is displayed in Fig. 9 at fixed  $q = 0.01 k_F$ . To demonstrate the importance of the interband effect, we compare the angular dependence on  $\phi_q$  with and without considering the interband transitions. In Fig. 9(a), the interband transition is turned off

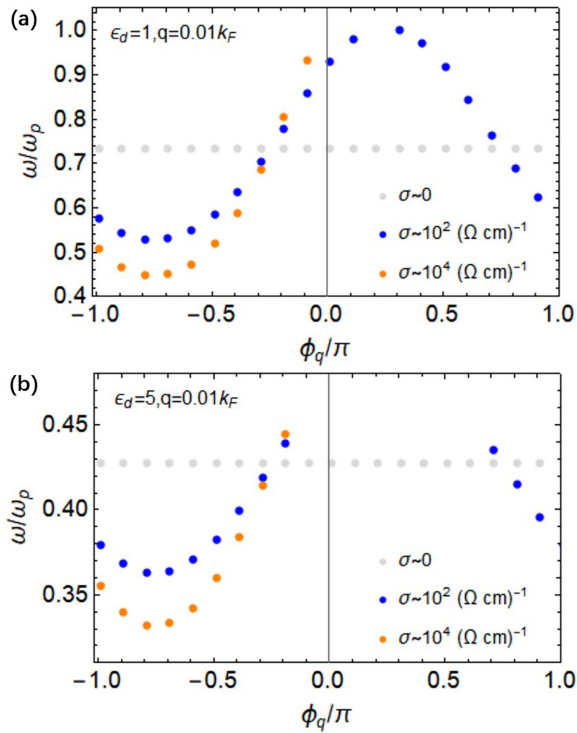


FIG. 9. Surface CBP frequency  $\omega$  as a function of  $\phi_q$  at a fixed  $q = 0.01 k_F$ . The effect of different value of AHC has been compared with [in (a) with  $\epsilon_d = 1$ ] and without [in (b) with  $\epsilon_d = 5$ ] the interband transitions.

( $\epsilon_d = 1$ ). The frequency exhibits a sinusoidal dependence on  $\phi_q$  for nonzero AHC and is equal to  $\omega_s = \omega_p/\sqrt{2}$  when  $\sigma_{\alpha\beta} = 0$ . As a qualitative demonstration,  $\sigma_{zx}$  and  $\sigma_{zy}$  has been set as the same value in solving Eq. (23). According to the Figs. 6 and 7,  $\omega$  is almost linearly dependent on  $q$ , we can thus use the long wavelength result (Eq. (25)) to understand the sinusoidal dependence on  $\phi_q$ . Take  $\omega_+$  as an example, it increases monotonically with the quantity of  $(\sigma_{zx} \cos \phi_q + \sigma_{zy} \sin \phi_q)$ . As  $\sigma_{zx} = \sigma_{zy} = \sigma$ , the quantity becomes  $\sqrt{2}\sigma \cos(\phi_q + \pi/4)$ , which has extrema at  $\phi_q = \pi/4$  or  $-3\pi/4$ , so is  $\omega$  as shown in Fig. 9(a). Another ratio of  $\sigma_{zx}$  to  $\sigma_{zy}$  will shift the extrema to a different angle  $\phi_q$ , which makes the angular dependence an interesting measurement for the anisotropy of AHC. Noting that the propagation direction of surface CBP is denoted by

$\phi_q$  rather than the sign of  $\omega$  in this figure,  $\omega$  has been taken positive values only. For an AHC above the threshold value, there is no forward propagating mode as explained in the discussion on Fig. 8.

As the interband transition is turned on, we have taken  $\epsilon_d = 5$  for an example, the surface CBP modes are completely forbidden to propagate in the directions of  $\phi_q$  between  $-0.1\pi$  and  $0.6\pi$ , even if the AHC is below the threshold. The presence of forbidden propagation directions of surface plasmons on the Py arises as result of  $\kappa$  becoming more likely to be pure imaginary as  $\epsilon_d$  increases. In the rest directions, the surface CBP frequency still depends on  $\phi_q$  sinusoidally with smaller extrema but at the same angle as in the  $\epsilon_d = 1$  case. The exhibition of forbidden direction is fully induced by the interband transitions, indicating the significance of the interband effect on the magnetic metals with occupied  $d$  bands like Py.

## V. CONCLUSION

To conclude, we have discussed the surface CBP on the disordered bulk Py. The main result is that there are two CBP modes on Py, whose frequency difference for a given wave vector can be enlarged by increasing the AHC, while the interband transition does the opposite. Above a threshold AHC, there is only one chiral mode left and always moving backward in the directions at an angle outside the forbidden range. Besides of being applied to devices that require nonreciprocity, there might be an interesting application in detecting the intrinsic AHC. For ferromagnetic metals, the intrinsic AHC is hard to be identified from experiments, since the side-jump contribution scales similarly to the intrinsic one. The additional scatterings between electrons with phonons and magnons make the situation even more complex. Surface CBP might be a potential indicator for the intrinsic AHC, whose anisotropy can be reflected by the phase of the sinusoidal dependence of the plasmon frequency on  $\phi_q$ .

## ACKNOWLEDGMENTS

The calculation was conducted on the High Performance Cluster at the Center for Joint Quantum Studies. This work was financially supported by the National Natural Science Foundation of China (11904256) and the National Key R&D Program of China (2021YFF1200700).

- [1] J. M. Pitarke, V. M. Silkin, E. V. Chulkov, and P. M. Echenique, Theory of surface plasmons and surface-plasmon polaritons, *Rep. Prog. Phys.* **70**, 1 (2007).
- [2] O. L. Berman, R. Y. Kezerashvili, and Y. E. Lozovik, Graphene-Based Photonics and Plasmonics, in *Nanoscale Materials and Devices for Electronics, Photonics and Solar Energy*, edited by A. Korkin, S. Goodnick, and R. Nemanich (Springer International Publishing, Cham, 2015), pp. 93–126.
- [3] A. S. Petrov, D. Svintsov, V. Ryzhii, and M. S. Shur, Amplified-reflection plasmon instabilities in grating-gate plasmonic crystals, *Phys. Rev. B* **95**, 045405 (2017).
- [4] V. Konopsky, V. Prokhorov, D. Lypenko, A. Dmitriev, E. Alieva, G. Dietler, and S. Sekatskii, Electrical excitation of long-range surface plasmons in PC/OLED structure with two metal nanolayers, *Nano-Micro Lett.* **12**, 35 (2020).
- [5] O. L. Berman, R. Y. Kezerashvili, and Y. E. Lozovik, Graphene nanoribbon based spaser, *Phys. Rev. B* **88**, 235424 (2013).
- [6] D. Zhang, Y. Zeng, Y. Bai, Z. Li, Y. Tian, and R. Li, Coherent surface plasmon polariton amplification via free-electron pumping, *Nature (London)* **611**, 55 (2022).
- [7] E. Ozbay, Plasmonics: Merging photonics and electronics at nanoscale dimensions, *Science* **311**, 189 (2006).

- [8] A. Tuniz, O. Bickerton, F. J. Diaz, T. Käsebier, E.-B. Kley, S. Kroker, S. Palomba, and C. M. de Sterke, Modular nonlinear hybrid plasmonic circuit, *Nat. Commun.* **11**, 2413 (2020).
- [9] O. L. Berman, Y. E. Lozovik, A. A. Kolesnikov, M. V. Bogdanova, and R. D. Coalson, Surface plasmon polaritons and optical transmission through a vortex lattice in a film of type-II superconductor, *J. Opt. Soc. Am. B* **30**, 909 (2013).
- [10] G. Gumbs, A. Iurov, D. Huang, and W. Pan, Tunable surface plasmon instability leading to emission of radiation, *J. Appl. Phys.* **118**, 054303 (2015).
- [11] A. Iurov, D. Huang, G. Gumbs, W. Pan, and A. A. Maradudin, Effects of optical polarization on hybridization of radiative and evanescent field modes, *Phys. Rev. B* **96**, 081408(R) (2017).
- [12] S. A. Diddams, K. Vahala, and T. Udem, Optical frequency combs: Coherently uniting the electromagnetic spectrum, *Science* **369**, eaay3676 (2020).
- [13] J. Rombaut, S. Martínez, U. M. Matera, P. Mazumder, and V. Pruneri, Antireflective multilayer surface with self-cleaning subwavelength structures, *ACS Photon.* **8**, 894 (2021).
- [14] G. X. Ni, H. Wang, J. S. Wu, Z. Fei, M. D. Goldflam, F. Keilmann, B. Özyilmaz, A. H. Castro Neto, X. M. Xie, M. M. Fogler, and D. N. Basov, Plasmons in graphene moiré superlattices, *Nat. Mater.* **14**, 1217 (2015).
- [15] S. A. A. Ghorashi, A. Dunbrack, A. Abouelkomsan, J. Sun, X. Du, and J. Cano, Topological and Stacked Flat Bands in Bilayer Graphene with a Superlattice Potential, *Phys. Rev. Lett.* **130**, 196201 (2023).
- [16] A. Iurov, G. Gumbs, and D. Huang, Many-body effects and optical properties of single and double layer  $\alpha$ - $T_3$  lattices, *J. Phys.: Condens. Matter* **32**, 415303 (2020).
- [17] A. Iurov, L. Zhemchuzhna, G. Gumbs, D. Huang, P. Fekete, F. Anwar, D. Dahal, and N. Weekes, Tailoring plasmon excitations in  $\alpha$ - $T_3$  armchair nanoribbons, *Sci. Rep.* **11**, 20577 (2021).
- [18] A. Iurov, L. Zhemchuzhna, G. Gumbs, D. Huang, D. Dahal, and Y. Abranyos, Finite-temperature plasmons, damping, and collective behavior in the  $\alpha$ - $T_3$  model, *Phys. Rev. B* **105**, 245414 (2022).
- [19] D. Pan, R. Yu, H. Xu, and F. J. García de Abajo, Topologically protected Dirac plasmons in a graphene superlattice, *Nat. Commun.* **8**, 1243 (2017).
- [20] D. Jin, T. Christensen, M. Soljačić, N. X. Fang, L. Lu, and X. Zhang, Infrared Topological Plasmons in Graphene, *Phys. Rev. Lett.* **118**, 245301 (2017).
- [21] J. C. W. Song and M. S. Rudner, Chiral plasmons without magnetic field, *Proc. Natl. Acad. Sci. USA* **113**, 4658 (2016).
- [22] D. Jalas, A. Petrov, M. Eich, W. Freude, S. Fan, Z. Yu, R. Baets, M. Popović, A. Melloni, J. D. Joannopoulos, M. Vanwolleghem, C. R. Doerr, and H. Renner, What is — and what is not — an optical isolator, *Nature Photon.* **7**, 579 (2013).
- [23] S. Mailis, On-chip non-magnetic optical isolator, *Nat. Photon.* **15**, 794 (2021).
- [24] S.-H. Yang, R. Naaman, Y. Paltiel, and S. S. P. Parkin, Chiral spintronics, *Nat. Rev. Phys.* **3**, 328 (2021).
- [25] M. E. McHenry and D. E. Laughlin, Magnetic Properties of Metals and Alloys, *Physical Metallurgy*, edited by D. E. Laughlin and K. Hono, 5th ed. (Elsevier, 2014), pp. 1881–2008.
- [26] M. Aoki, E. Shigematsu, R. Ohshima, T. Shinjo, M. Shiraishi, and Y. Ando, Anomalous sign inversion of spin-orbit torque in ferromagnetic/nonmagnetic bilayer systems due to self-induced spin-orbit torque, *Phys. Rev. B* **106**, 174418 (2022).
- [27] S. P. Bommanaboyena, D. Backes, L. S. I. Veiga, S. S. Dhesi, Y. R. Niu, B. Sarpi, T. Denneulin, A. Kovács, T. Mashoff, O. Gomonay, J. Sinova, K. Everschor-Sitte, D. Schönke, R. M. Reeve, M. Kläui, H.-J. Elmers, and M. Jourdan, Readout of an antiferromagnetic spintronics system by strong exchange coupling of  $Mn_2Au$  and Permalloy, *Nat. Commun.* **12**, 6539 (2021).
- [28] T. Manoj, S. Kotha, B. Paikaray, D. Srideep, A. Haldar, K. V. Rao, and C. Murapaka, Giant spin pumping at the ferromagnet (permalloy) – organic semiconductor (perylene diimide) interface, *RSC Adv.* **11**, 35567 (2021).
- [29] H. Bangar, A. Kumar, N. Chowdhury, R. Mudgal, P. Gupta, R. S. Yadav, S. Das, and P. K. Muduli, Large spin-to-charge conversion at the two-dimensional interface of transition-metal dichalcogenides and permalloy, *ACS Appl. Mater. Interfaces* **14**, 41598 (2022).
- [30] H. Arava, F. Barrows, M. D. Stiles, and A. K. Petford-Long, Topological control of magnetic textures, *Phys. Rev. B* **103**, L060407 (2021).
- [31] V. Brajuskovic and C. Phatak, Understanding curvature effects on the magnetization reversal of patterned permalloy Archimedean spirals, *Appl. Phys. Lett.* **118**, 152409 (2021).
- [32] B. L. Le, J. Park, J. Sklenar, G.-W. Chern, C. Nisoli, J. D. Watts, M. Manno, D. W. Rench, N. Samarth, C. Leighton, and P. Schiffer, Understanding magnetotransport signatures in networks of connected permalloy nanowires, *Phys. Rev. B* **95**, 060405(R) (2017).
- [33] W. Fonseca, F. Garcia, F. Caravelli, and C. de Araujo, Memristive Effects in Nanopatterned Permalloy Kagomé Array, *Phys. Rev. Appl.* **18**, 014070 (2022).
- [34] Q. Li, S. Xiong, L. Chen, K. Zhou, R. Xiang, H. Li, Z. Gao, R. Liu, and Y. Du, Spin-wave dynamics in an artificial kagome spin ice, *Chinese Phys. Lett.* **38**, 047501 (2021).
- [35] S. S.-L. Zhang and G. Vignale, Chiral surface and edge plasmons in ferromagnetic conductors, *Phys. Rev. B* **97**, 224408 (2018).
- [36] A. Liebsch, *Electronic Excitations at Metal Surfaces* (Springer US, Boston, MA, 1997).
- [37] A. Van Itterbeek, A. Dupré, and G. Brandt, Resistivity measurements on permalloy films, *Appl. Sci. Res.* **9**, 470 (1961).
- [38] J.-H. Park, H.-W. Ko, J.-M. Kim, J. Park, S.-Y. Park, Y. Jo, B.-G. Park, S. K. Kim, K.-J. Lee, and K.-J. Kim, Temperature dependence of intrinsic and extrinsic contributions to anisotropic magnetoresistance, *Sci. Rep.* **11**, 20884 (2021).
- [39] D. Xiao, M.-C. Chang, and Q. Niu, Berry phase effects on electronic properties, *Rev. Mod. Phys.* **82**, 1959 (2010).
- [40] Y. Yao, L. Kleinman, A. H. MacDonald, J. Sinova, T. Jungwirth, D.-s. Wang, E. Wang, and Q. Niu, First Principles Calculation of Anomalous Hall Conductivity in Ferromagnetic bcc Fe, *Phys. Rev. Lett.* **92**, 037204 (2004).
- [41] X. Wang, J. R. Yates, I. Souza, and D. Vanderbilt, *Ab Initio* calculation of the anomalous Hall conductivity by Wannier interpolation, *Phys. Rev. B* **74**, 195118 (2006).
- [42] A. van de Walle, M. Asta, and G. Ceder, The alloy theoretic automated toolkit: A user guide, *Calphad* **26**, 539 (2002).
- [43] A. van de Walle, P. Tiwary, M. de Jong, D. Olmsted, M. Asta, A. Dick, D. Shin, Y. Wang, L.-Q. Chen, and Z.-K. Liu, Efficient stochastic generation of special quasirandom structures, *Calphad* **42**, 13 (2013).

- [44] J. Zhang, Y.-P. Zhang, and C.-M. Su, First-principles study of  $\text{FeNi}_{1-x}\text{Cr}_x$  ( $0 \leq x \leq 1$ ) disordered alloys from special quasirandom structures, *Calphad* **71**, 102007 (2020).
- [45] G. Nahrwold, J. M. Scholtyssek, S. Motl-Ziegler, O. Albrecht, U. Merkt, and G. Meier, Structural, magnetic, and transport properties of Permalloy for spintronic experiments, *J. Appl. Phys.* **108**, 013907 (2010).
- [46] D. M. C. Nicholson, W. H. Butler, W. A. Shelton, Y. Wang, X.-G. Zhang, G. M. Stocks, and J. M. MacLaren, Magnetic structure and electronic transport in permalloy, *J. Appl. Phys.* **81**, 4023 (1997).
- [47] N. Ghosh, H. Das, M. Gafur, and A. A. Hossain, Formation and magnetic properties of nanocrystalline 78.5-permalloy by mechanical alloying, *Procedia Eng.* **90**, 136 (2014).
- [48] G. Kresse and J. Furthmüller, Efficient iterative schemes for *ab initio* total-energy calculations using a plane-wave basis set, *Phys. Rev. B* **54**, 11169 (1996).
- [49] G. Kresse and D. Joubert, From ultrasoft pseudopotentials to the projector augmented-wave method, *Phys. Rev. B* **59**, 1758 (1999).
- [50] B. Hammer, L. B. Hansen, and J. K. Nørskov, Improved adsorption energetics within density-functional theory using revised Perdew-Burke-Ernzerhof functionals, *Phys. Rev. B* **59**, 7413 (1999).
- [51] J. P. Perdew, J. A. Chevary, S. H. Vosko, K. A. Jackson, M. R. Pederson, D. J. Singh, and C. Fiolhais, Atoms, molecules, solids, and surfaces: Applications of the generalized gradient approximation for exchange and correlation, *Phys. Rev. B* **46**, 6671 (1992).
- [52] H. J. Monkhorst and J. D. Pack, Special points for Brillouin-zone integrations, *Phys. Rev. B* **13**, 5188 (1976).
- [53] M. Gajdoš, K. Hummer, G. Kresse, J. Furthmüller, and F. Bechstedt, Linear optical properties in the projector-augmented wave methodology, *Phys. Rev. B* **73**, 045112 (2006).
- [54] A. A. Mostofi, J. R. Yates, Y.-S. Lee, I. Souza, D. Vanderbilt, and N. Marzari, Wannier90: A tool for obtaining maximally-localised Wannier functions, *Comput. Phys. Commun.* **178**, 685 (2008).
- [55] Q. Wu, S. Zhang, H.-F. Song, M. Troyer, and A. A. Soluyanov, WannierTools: An open-source software package for novel topological materials, *Comput. Phys. Commun.* **224**, 405 (2018).
- [56] S. L. Adler, Quantum theory of the dielectric constant in real solids, *Phys. Rev.* **126**, 413 (1962).
- [57] N. Wiser, Dielectric constant with local field effects included, *Phys. Rev.* **129**, 62 (1963).
- [58] M. Zhang and C. Deng, Magnetic, optical and electrical properties of permalloy films by DC magnetron sputtering, *J Mater Sci: Mater Electron* **32**, 4949 (2021).
- [59] M. J. van Setten, S. Er, G. Brocks, R. A. de Groot, and G. A. de Wijs, First-principles study of the optical properties of  $\text{Mg}_x\text{Ti}_{1-x}\text{H}_2$ , *Phys. Rev. B* **79**, 125117 (2009).
- [60] L. Ye, Y. Tian, X. Jin, and D. Xiao, Temperature dependence of the intrinsic anomalous Hall effect in nickel, *Phys. Rev. B* **85**, 220403(R) (2012).
- [61] Y. Q. Zhang, N. Y. Sun, R. Shan, J. W. Zhang, S. M. Zhou, Z. Shi, and G. Y. Guo, Anomalous Hall effect in epitaxial permalloy thin films, *J. Appl. Phys.* **114**, 163714 (2013).